Giant Cross–Kerr Effect for Propagating Microwaves Induced by an Artificial Atom

Io-Chun Hoi,[1] Anton F. Kockum,[1] Tauno Palomaki,[1] Thomas M. Stace,[2] Bixuan Fan,[2] Lars Tornberg,[1]
Sankar R. Sathyamoorthy,[1] Göran Johansson,[1] Per Delsing,[1,*] and C. M. Wilson[1,3,†]

[1]*Department of Microtechnology and Nanoscience (MC2), Chalmers University of Technology, SE-412 96 Göteborg, Sweden*
[2]*Centre for Engineered Quantum Systems, School of Physical Sciences, University of Queensland,*
Saint Lucia, Queensland 4072, Australia
[3]*Institute for Quantum Computing and Electrical and Computer Engineering Department, University of Waterloo,*
Waterloo N2L 3G1, Canada

We investigate the effective interaction between two microwave fields, mediated by a transmon-type superconducting artificial atom which is strongly coupled to a coplanar transmission line. The interaction between the fields and atom produces an effective cross–Kerr coupling. We demonstrate average cross–Kerr phase shifts of up to 20 degrees per photon with both coherent microwave fields at the single-photon level. Our results provide an important step toward quantum applications with propagating microwave photons.

PACS numbers: 42.50.Gy, 42.50.Pq, 42.65.Hw, 85.25.Cp

In recent years, there has been great interest in using photons as quantum bits for quantum information processing [1]. The implementation of quantum logic gates using photons requires interactions between two fields [1,2]. One possible coupling mechanism is the Kerr effect, where the photons interact via a nonlinear medium. By means of the Kerr effect, quantum logic operations such as the controlled phase gate [3], the quantum Fredkin gate [4] and the conditional phase switch [5] can be realized. Moreover, quantum nondemolition (QND) detection of propagating photons using the Kerr phase shift has been discussed in the literature [6]. Superconducting qubits provide a very strong nonlinearity [7,8] that might be suitable for this purpose.

In cavity QED experiments, Kerr phase shifts on the order of 10 degrees have been measured at the single-photon level [9]. However, in this configuration, the presence of the cavity limits the bandwidth, which constrains its usefulness over a wide range of frequencies. Therefore an open quantum system without a cavity is advantageous. An example of such a system is atoms coupled to a one-dimensional electromagnetic environment. A Kerr phase shift is also present in these systems, but so far the measured phase shift has been very small. In nonlinear photonic crystal fibers, for instance, an average Kerr phase shift of 10^{-2} degrees per photon has been measured [10,11]. A new class of open quantum systems has been made possible by progress in *circuit* QED, providing a fascinating platform for engineering light-atom interactions [12–19] and testing fundamental aspects of quantum physics [20]. For instance, the generation of nonclassical states exhibiting photon antibunching has recently been demonstrated in such an open quantum system [21–23].

In this Letter, we realize a cross–Kerr interaction between two microwave fields by coupling a superconducting artificial atom, known as a transmon [24], to an open transmission line. We employ two device configurations:

device 1 [Fig. 1(a)] has a transmon in an open transmission line [7,8,21], and device 2 [Fig. 1(b)] has a transmon at the end of a transmission line. Due to the strong coupling between atom and field, we achieve average phase shifts up to 10 and 20 degrees per photon at the single-photon level for devices 1 and 2, respectively. This is several orders of magnitude larger than in optical systems [10,11]. We stress that the Kerr effect demonstrated here is purely due to the coherent interaction between the fields and the transmon. This differs greatly from what has previously been demonstrated in superconducting devices where utilization of the kinetic inductance of a superconducting film [25] or the Josephson inductance of a superconducting quantum interference device (SQUID) [26] requires a pump tone power at least several orders of magnitude higher than those used in this experiment.

The transmon is strongly coupled through a capacitance C_c to a one-dimensional transmission line with a characteristic impedance of $Z_0 = 50\ \Omega$. An external magnetic flux allows us to tune the frequencies $\omega_{10} = E_1 - E_0$ and $\omega_{21} = E_2 - E_1$ of the allowed dipole transitions of the transmon. From a theoretical point of view, devices 1 and 2 are essentially the same, with one difference: the emitted field from the transmon can propagate in two directions for device 1, but only in one direction for device 2 since it is placed at the end of the transmission line. In the context of quantum measurement, we anticipate that it may be beneficial to have all information confined to a single channel (device 2), instead of distributed between two (device 1). Moreover, as we will show later, we find that device 2 is a better Kerr medium. For both devices, the photon-photon interaction is mediated by the three-level transmon. We apply two continuous tones, the probe at $\omega_p \approx \omega_{10}$ and the control at $\omega_c = \omega_{21}$ [see Fig. 1(c)]. We observe the induced amplitude and phase shift of the probe as the control tone is turned on and off. The response depends
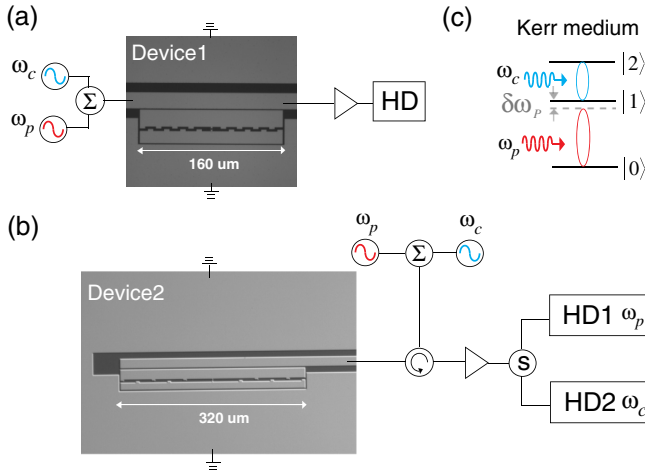
FIG. 1 (color online). A micrograph of device 1 in (a) and device 2 in (b) with measurement setup using heterodyne detection (HD). Devices 1 and 2 have an artificial atom, a transmon qubit, embedded in a one-dimensional open transmission line and at the end of a transmission line, respectively. In (b), we measure the reflection coefficient of the probe and control fields simultaneously. (c) The three-level artificial atom driven by a probe tone at ω_p (red) and a control tone at ω_c (blue). The artificial atom acts as a Kerr medium, which enables photon-photon interaction.

on the powers and the detunings of the probe and the control tones. In the following, we quantify the effect of these parameters on the response.

The electromagnetic field in the transmission line can be described by the complex voltage amplitudes for the incoming field, V_{in}, and the resulting transmitted and reflected fields, V_T and V_R respectively. For device 1, we then define the complex transmission and reflection coefficients as $t_p = \langle V_T \rangle / \langle V_{\text{in}} \rangle$ and $r_p = \langle V_R \rangle / \langle V_{\text{in}} \rangle$, respectively, where $\langle x \rangle = T_m^{-1} \int_0^{T_m} d\tau x(\tau)$ denotes averaging over the measurement time, T_m. Thus, t_p and r_p measure the phase coherent signal. Some of the input signal is incoherently transmitted or reflected, such that $|r_p|^2 + |t_p|^2 < 1$. Importantly, this does *not* necessarily imply any power dissipation in the device. In particular, the portions of the reflected and transmitted signals resulting from spontaneous emission average to zero in $\langle V_T \rangle$ and $\langle V_R \rangle$.

We first characterize the devices spectroscopically. The response of both devices is qualitatively similar, so for clarity, we describe that of device 1 in more detail. Results for device 2 are presented in the Supplemental Material. Device 1 is characterized by measuring t_p as a function of probe frequency, ω_p, at low probe power, P_p. The extinction dip provides the $|0\rangle \leftrightarrow |1\rangle$ transition frequency. The $|1\rangle \leftrightarrow |2\rangle$ transition can then be directly measured using two-tone spectroscopy [8]. We extract $\omega_{10}/2\pi = 7.10\,\text{GHz}$ and $\omega_{21}/2\pi = 6.38$ GHz, giving an anharmonicity of $\alpha/2\pi = 720$ MHz between the two transitions.

We can then explore the two-tone response in more detail. A coherent probe (control) signal will drive coherent

oscillations of the $|0\rangle \leftrightarrow |1\rangle$ ($|1\rangle \leftrightarrow |2\rangle$) dipole at a Rabi frequency, Ω_p (Ω_c), which is linear in the probe (control) amplitude. Figure 2(a) shows the magnitude (top) and phase (bottom) of t_p for device 1 with control on, $t_p^{(\text{on})}$, and control off, $t_p^{(\text{off})}$. We can clearly see the formation of the Autler-Townes doublet in $|t_p^{(\text{on})}|$ [28,29]. The doublet states appear as a pair of minima in the black curves of Fig. 2(a) with a separation given by Ω_c.

Figure 2(b) shows the measured amplitude response, Δt_p, defined as the difference between the magnitude of the probe transmission $\Delta t_p = |t_p^{(\text{on})}| - |t_p^{(\text{off})}|$. Figure 2(c) shows the corresponding phase response, $\Delta\varphi_p$. For these measurements the probe Rabi frequency, Ω_p, is much less than the 1-0 decoherence rate, γ_{10}. The solid curves in the lower panels are calculated using a Lindblad master equation for an open, driven, three-level system [28,30]. This model includes parameters representing the relaxation rates Γ_{10}, the pure dephasing rate $\Gamma_{\phi,10}$ for the coherence between $|0\rangle$ and $|1\rangle$, and the 2-0 decoherence rate, γ_{20} [28,30]. The values for these parameters are given in the caption. From these, we calculate the decoherence rate $\gamma_{10} = \Gamma_{10}/2 + \Gamma_{\phi,10}$. As expected, the maximum induced amplitude response occurs when the probe is on resonance, and the induced phase response is maximized when the probe is detuned from resonance by an amount $\delta\omega_p = \omega_p - \omega_{10} \approx 2\pi \times 20$ MHz.

Quantum applications of cross–Kerr media typically require large phase shifts at the single-photon level. Therefore, we now quantify the cross–Kerr phase shift in the limit of low control power [31]. In this limit, the cross–Kerr phase shift is given by $\Delta\varphi_p = kP_c$, where k is the Kerr coefficient. To convert this to a phase shift per control photon, we note that the average number of control photons $\langle N_c \rangle$ per interaction time, $2\pi/\Gamma_{21}$, is given by $\langle N_c \rangle = 2\pi P_c/(\hbar\omega_c\Gamma_{21})$, so $\Delta\varphi_p$ is proportional to $\langle N_c \rangle$. For reference, $\langle N_c \rangle = 1$ corresponds to $P_c = -122$ dBm ($= 0.64\,\text{fW}$) and $\langle N_p \rangle = 1$ corresponds to $P_p = -124.5$ dBm for device 1, with $P_c = -123.4$ dBm and $P_p = -126$ dBm the corresponding numbers for device 2.

Figure 3(b) shows the probe phase response, $\Delta\varphi_p$, as a function of probe frequency for several very weak probe powers (with a control power of $P_c = -127$ dBm, i.e., $\langle N_c \rangle \simeq 0.3$). As in Fig. 2(c), the maximum phase shift occurs at a probe detuning of $\delta\omega_p/2\pi \approx 20$ MHz. At this point, we measure $\Delta\varphi_p$ as a function of $\langle N_c \rangle$, with the results shown in Fig. 3(c). For $\langle N_c \rangle = 1$, we observe a phase shift of approximately 20 degrees for device 2 and 10 degrees for device 1 [32].

To further characterize the response of device 2, Fig. 3(d) shows the corresponding magnitudes $|r_{p,2}|$ and $|r_{c,2}|$ as a function of $\langle N_c \rangle$. Here we use the additional subscript "2" to distinguish the coefficients for device 2, which have a different functional form than for device 1. The dependence
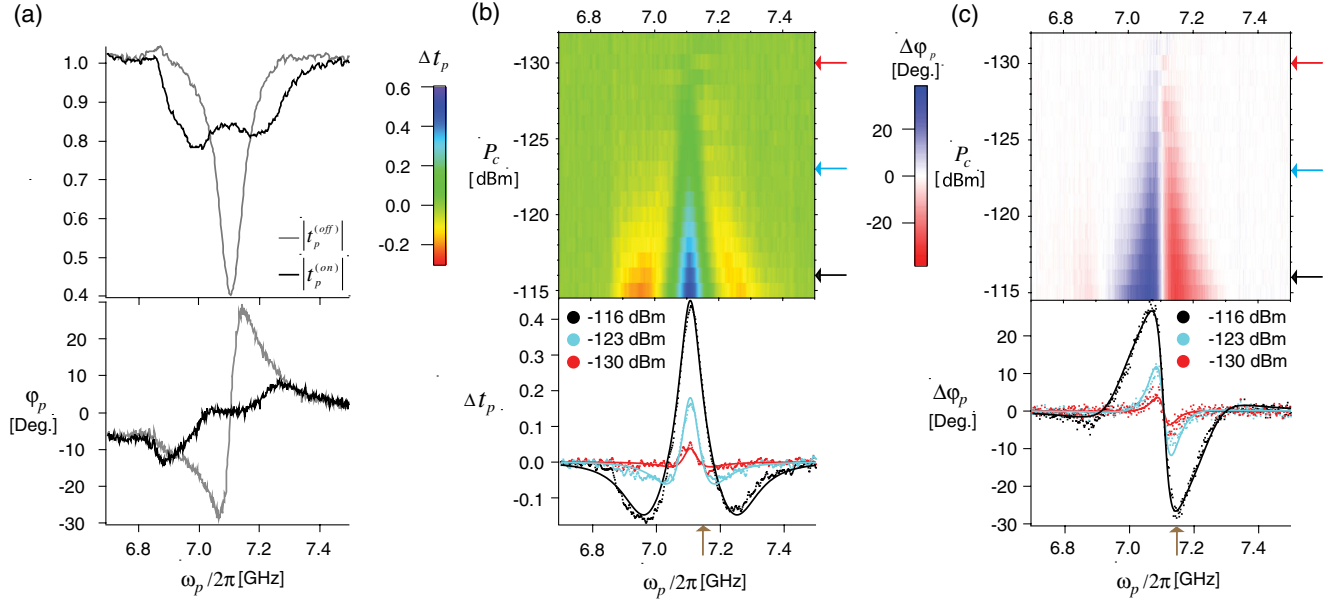
FIG. 2 (color online).　Transmission coefficient for the probe, as a function of ω_p and control power, P_c, for low probe powers, $\Omega_p \ll \gamma_{10}$ in device 1 (see the Supplemental Material for device 2). (a) Top: measured transmission coefficient with $P_c = -116$ dBm, $|t_p^{(on)}|$ (black), and P_c turned off, $|t_p^{(off)}|$ (gray). Bottom: corresponding phase response. (b) Measured amplitude response, Δt_p. (c) Measured phase response, $\Delta \varphi_p$. Top panels: as a function of probe frequency and control power. Bottom panels: horizontal line cuts (dots) and theory curves (solid lines). The (brown) arrows along the bottom axes show the frequency that maximizes the phase response. The theory curves [28,30] are fit simultaneously to extract $\gamma_{20}/2\pi = 150$ MHz along with the control field coupling. The following other parameters, also used in the calculations, are independently measured with single-tone and two-tone spectroscopy: $\omega_{10}/2\pi = 7.10$ GHz, $\omega_{21}/2\pi = 6.38$ GHz, $\Gamma_{10}/2\pi = 74$ MHz, $\gamma_{10}/2\pi = 60$ MHz and the probe field coupling.
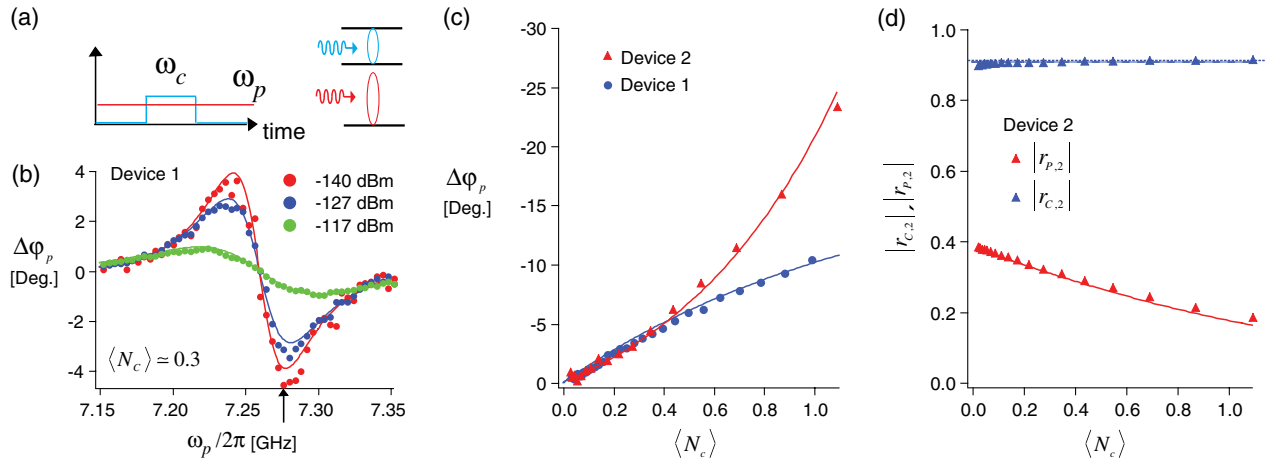

FIG. 3 (color online).　Probe phase shift, $\Delta \varphi_p$, induced by a weak control pulse. Solid curves are theoretical fits to the data, including additional data in the Supplemental Material. The fitting parameters for each device are γ_{20} and the control field coupling. Other parameters are measured independently through spectroscopy. All parameters are listed in Table I. (a) The control pulse induces a phase shift, $\Delta \varphi_p$, of the continuous probe in the time domain. The length of the pulse is 1 μs for device 1 and 7 μs for device 2. (b) $\Delta \varphi_p$ as a function of ω_p for three different probe powers and $\langle N_c \rangle \simeq 0.3$, for device 1. Note that here the $|0\rangle \leftrightarrow |1\rangle$ transition is 7.26 GHz (due to a different external magnetic flux, Φ). (c) $\Delta \varphi_p$ as a function of $\langle N_c \rangle$ for a weak probe at a probe frequency that maximizes the probe phase shift. Each data point is an average over 2 million control pulses. An average phase shift of 10 degrees per control photon is observed in device 1, and 20 degrees per control photon in device 2. (d) $|r_{p,2}|$ and $|r_{c,2}|$ as a function of $\langle N_c \rangle$. The dashed (blue) line indicates $|r_{c,2}| = 0.9$. Extensive measurements of $r_{p,2}$ are presented in Fig. S4A of the Supplemental Material [27].

TABLE I.   Parameters for device 1, 2. The first six parameters, labeled "Spectroscopic," are determined from single-tone and two-tone spectroscopy. The parameter γ_{20} is extracted from fitting the Kerr data in Fig. 3. These seven parameters are used to derive the remaining quantities. All dimensionful quantities are in gigahertz. Note that some parameters for device 1 are different than in Fig. 2 because the device was operated at a different flux bias.

| Device | Spectroscopic | | | | | | Kerr | Derived | | | | |
	E_J/h	E_C/h	$\omega_{10}/2\pi$	$\omega_{21}/2\pi$	$\Gamma_{10}/2\pi$	$\Gamma_{\phi,10}/2\pi$	$\gamma_{20}/2\pi$	$\Gamma_{21}/2\pi$	$\gamma_{10}/2\pi$	E_J/E_C	$\delta\omega_p/2\pi$	$|\Delta\varphi_p/\langle N_c\rangle|$
1	13.1	0.59	7.26	6.54	0.074	0.020	0.160	0.148	0.057	22.2	0.02	10°
2	11.99	0.42	5.916	5.50	0.063	0.015	0.093	0.126	0.047	28.5	0.009	20°

of $|r_{p,2}|$ and $|r_{c,2}|$ on $\langle N_c\rangle$ can be understood in terms of dephasing. For device 2 (Fig. 1(b)), the reflection coefficient is defined as $r_{p,2} = \langle V_R\rangle/\langle V_{in}\rangle$ where V_R is the sum of the incoming field and the field emitted by the transmon. We then find $r_{p,2} = 1 + 2i(\Gamma_{10}/\Omega_p)\langle\sigma_-\rangle$, where $\sigma_- = |0\rangle\langle 1|$ is the atomic lowering operator. The factor of 2 in the 2nd term is a consequence of having only one emission channel for the atom. For a weak resonant probe ($\omega_p = \omega_{10}$, $\Omega_p \ll \gamma_{10}$), we find the following expression [33]:

$$|r_{p,2}| = \left| 1 - \frac{2}{1 + 2\Gamma_{\phi,10}/\Gamma_{10}} \right|. \quad (1)$$

In Fig. 3(d), for a fixed $\delta\omega_p/2\pi \approx 9$ MHz, the low control-power limit of $|r_{p,2}| \approx 0.4$ is determined by $\Gamma_{\phi,10}$ and Γ_{10}. As $\langle N_c\rangle$ increases, we see that $|r_{p,2}|$ decreases. This effect is due to the power broadening of the linewidth of state $|1\rangle$ induced by the control tone, which effectively increases the dephasing rate. Therefore, with phase-sensitive detection, the coherent signal $|r_{p,2}|$ becomes weaker as $\langle N_c\rangle$ increases. We also see $|r_{c,2}| \sim 0.90$ is relatively constant, though it increases to unity as the transition saturates at high power, $\Omega_c \gg \gamma_{21}$. With a weak probe, $\Omega_p \ll \gamma_{10}$, there is a low probability of the atom being in the first excited state. As a result, the probability of the atom scattering a control photon is very low, and the dephasing is small. Note that the reduction of $|r_{p,2}|$ and $|r_{c,2}|$ in Fig. 3(d) is not due to dissipation but instead due to a loss of phase coherence in the signal. Indeed, both $\langle N_c\rangle$ and $\langle N_p\rangle$ are conserved, which has been confirmed in our previous work [21,34].

We have demonstrated a Kerr medium working in the semiclassical regime, showing good performance and good agreement with theory. Cross–Kerr media have long been proposed for quantum applications such as the QND measurement of photon number [6]. Therefore, it is interesting to estimate what the performance of the device would be in this application. To achieve QND photon counting, the phase shift of the probe produced by a single photon in the control mode (i.e., the signal) must be resolved above the probe phase noise, that is, the signal-to-noise ratio (SNR) should be greater than 1. Following the approach of Ref. [35] (see the Supplemental Material), we calculate the optimum SNR using the parameters of device 2.

We consider also whether the performance is enhanced by exchanging the role of probe and control. In fact, we find this arrangement ($\omega_p \approx \omega_{21}$ and $\omega_c \approx \omega_{10}$) to be best, giving a SNR of 0.38 measuring a single-photon Fock state and assuming the only noise is vacuum noise. (With the probe and control as in Fig. 3, the SNR is about a factor of 2 lower.) However, as discussed in Ref. [35], due to a subtle interplay between transmon saturation and vacuum noise, the probe phase noise for a single transmon *always* dominates the cross–Kerr-induced phase shift, and it is found that SNR $\lesssim 0.6$ under very general assumptions. Thus, our device is quite close to the theoretical optimum for cross–Kerr phase shifts. It, therefore, potentially offers an important platform on which to test proposals for cross–Kerr based protocols.

In conclusion, we have investigated the nonlinear interaction between two microwave fields at the single-photon level induced by a three-level superconducting transmon. In particular, we observed an average cross Kerr phase shift of 20 degrees per photon between two coherent microwave fields. Compared to cavity-based systems [36], this system has the advantage of being tunable *in situ* over a wide range of frequencies. Such giant Kerr phase shifts may find applications in quantum information applications.

*per.delsing@chalmers.se
†chris.wilson@uwaterloo.ca

[1] E. Knill, R. Laflamme, and G. J. Milburn, Nature (London) **409**, 46 (2001).
[2] J. H. Shapiro and M. Razavi, New J. Phys. **9**, 16 (2007).
[3] Q. A. Turchette, C. J. Hood, W. Lange, H. Mabuchi, and H. J. Kimble, Phys. Rev. Lett. **75**, 4710 (1995).
[4] G. J. Milburn, Phys. Rev. Lett. **62**, 2124 (1989).
[5] K. J. Resch, J. S. Lundeen, and A. M. Steinberg, Phys. Rev. Lett. **89**, 037904 (2002).

[6] W. J. Munro, K. Nemoto, R. G. Beausoleil, and T. P. Spiller, Phys. Rev. A **71**, 033819 (2005).

[7] O. Astafiev, A. M. Zagoskin, A. A. Abdumalikov, Y. A. Pashkin, T. Yamamoto, K. Inomata, Y. Nakamura, and J. S. Tsai, Science **327**, 840 (2010).

[8] I.-C. Hoi, C. M. Wilson, G. Johansson, T. Palomaki, B. Peropadre, and P. Delsing, Phys. Rev. Lett. **107**, 073601 (2011).

[9] I. Fushman, D. Englund, A. Faraon, N. Stoltz, P. Petroff, and J. Vuckovic, Science **320**, 769 (2008).

[10] N. Matsuda, R. Shimizuand, Y. Mitsumori, H. Kosaka, and K. Edamatsu, Nat. Photonics **3**, 95 (2009).

[11] V. Venkataraman, K. Saha, and A. L. Gaeta, Nat. Photonics **7**, 138 (2012); C. Perrella, P. S. Light, J. D. Anstie, F. Benabid, T. M. Stace, A. G. White, and A. N. Luiten, Phys. Rev. A **88**, 013819 (2013).

[12] Y. Nakamura, Y. A. Pashkin, and J. S. Tsai, Nature (London) **398**, 786 (1999).

[13] D. Vion, A. Aassime, A. Cottet, P. Joyez, H. Pothier, C. Urbina, D. Esteve, and M. H. Devoret, Science **296** 886 (2002).

[14] A. Wallraff, D. I. Schuster, A. Blais, L. Frunzio, R. S. Huang, J. Majer, S. Kumar, S. M. Girvin, and R. J. Schoelkopf, Nature (London) **431**, 162 (2004).

[15] M. Hofheinz, H. Wang, M. Ansmann, R. C. Bialczak, E. Lucero, M. Neeley, A. D. O'Connell, D. Sank, J. Wenner, J. M. Martinis *et al.*, Nature (London) **459**, 546 (2009).

[16] C. M. Wilson, T. Duty, F. Persson, M. Sandberg, G. Johansson, and P. Delsing, Phys. Rev. Lett. **98**, 257003 (2007).

[17] M. Sandberg, F. Persson, I. C. Hoi, C. M. Wilson, and P. Delsing, Phys. Scr. **T137**, 014018 (2009).

[18] M. U. Staudt, I.-C. Hoi, P. Krantz, M. Sandberg, M. Simoen, P. Bushev, N. Sangouard, M. Afzelius, V. S. Shumeiko, G. Johansson *et al.*, J. Phys. B **45**, 124019 (2012).

[19] D. Bozyigit, C. Lang, L. Steffen, J. M. Fink, C. Eichler, M. Baur, R. Bianchetti, P. J. Leek, S. Filipp, M. P. da Silva *et al.*, Nat. Phys. **7**, 154 (2011).

[20] C. M. Wilson, G. Johansson, A. Pourkabirian, M. Simoen, J. R. Johansson, T. Duty, F. Nori, and P. Delsing, Nature (London) **479**, 376 (2011).

[21] I.-C. Hoi, T. Palomaki, J. Lindkvist, G. Johansson, P. Delsing, and C. M. Wilson, Phys. Rev. Lett. **108**, 263601 (2012).

[22] H. J. Carmichael, Phys. Rev. Lett. **70**, 2273 (1993).

[23] D. E. Chang, A. S. Sorensen, E. A. Demler, and M. D. Lukin, Nat. Phys. **3**, 807 (2007).

[24] J. Koch, T. M. Yu, J. Gambetta, A. A. Houck, D. I. Schuster, J. Majer, A. Blais, M. H. Devoret, S. M. Girvin, and R. J. Schoelkopf, Phys. Rev. A **76**, 042319 (2007).

[25] E. A. Tholén, A. Ergül, E. M. Doherty, F. M. Weber, F. Grégis, and D. B. Haviland, Appl. Phys. Lett. **90**, 253509 (2007).

[26] M. A. Castellanos-Beltran, K. D. Iwin, L. R. Vale, G. C. Hilton, and K. W. Lehnert, IEEE Trans. Appl. Supercond. **19**, 944 (2009).

[27] See the Supplemental Material http://link.aps.org/supplemental/10.1103/PhysRevLett.111.053601 for additional supporting data and a description of the theoretical model used to estimate the single-photon detection efficiency.

[28] A. A. Abdumalikov, O. Astafiev, A. M. Zagoskin, Y. A. Pashkin, Y. Nakamura, and J. S. Tsai, Phys. Rev. Lett. **104**, 193601 (2010).

[29] S. H. Autler and C. H. Townes, Phys. Rev. **100**, 703 (1955).

[30] B. Peropadre, J. Lindkvist, I.-C. Hoi, C. M. Wilson, J. J. Garcia-Ripoll, P. Delsing, and G. Johansson, New J. Phys. **15**, 035009 (2013).

[31] H. Schmidt and A. Imamoglu, Opt. Lett. **21**, 1936 (1996).

[32] We comment that there is a systematic uncertainty, of order 20%, in the calibration of $\langle N_c \rangle$ for device 1 in Fig. 3(c). For small probe and control powers, the parameters γ_{20} and Ω_c cannot be determined independently with high precision. At high control powers, the resolved Autler-Townes splitting enables an independent calibration of Ω_c. This high-power calibration was unfortunately not repeated for device 1 for the flux-bias point in Fig. 3. It was, however, done for device 2.

[33] K. Koshino and Y. Nakamura, New J. Phys. **14**, 043005 (2012).

[34] I.-C. Hoi, C. M. Wilson, G. Johansson, J. Lindkvist, B. Peropadre, T. Palomaki, and P. Delsing, New J. Phys. **15**, 025011 (2013).

[35] B. Fan, A. F. Kockum, J. Combes, G. Johansson, I.-C. Hoi, C. M. Wilson, P. Delsing, G. J. Milburn, and T. M. Stace, Phys. Rev. Lett. **110**, 053601 (2013).

[36] S. Rebic, J. Twamley, and G. J. Milburn, Phys. Rev. Lett. **103**, 150503 (2009).